TIME-RESOLVED STEREO PIV MEASUREMENTS OF AN ACTIVE GURNEY FLAP SYSTEM

Stefan van 't Hoff
NLR
A. Fokkerweg 2, Amsterdam, 1006 BM
The Netherlands

Marthijn Tuinstra
NLR
A. Fokkerweg 2, Amsterdam, 1006 BM
The Netherlands

Abstract

This paper presents the results of the Particle Image Velocimetry (PIV) measurements performed during the full-scale two-dimensional Active Gurney Flap (AGF) wind tunnel test campaign executed early 2014 as part of the Innovative Rotor Blades work package of the European Clean Sky – Green Rotorcraft initiative. The test article consisted of a main rotor blade section featuring a modified public domain airfoil fitted with a full-span AGF, driven by a flight representative actuator and mechanism. The objective of the test was to improve the understanding of the flow physics of a dynamically deploying upstream AGF, to provide a basis for the validation of numerical models and to serve as an integrated functionality test of the AGF actuator and mechanism. Besides forming a necessary stepping stone towards the rotor and flight test activities scheduled in the continuation of the project, the novelty of the test campaign lies in the time-resolved PIV measurements performed on an actively deploying upstream AGF. Two separate PIV camera arrangements were employed, one focusing on the direct vicinity of the AGF and one focusing on the shed wake behind the airfoil. Both sinusoidal and ramp-type deployments were considered at different deployment heights and frequencies. The first part of the paper presents the background and motivation of the test activities and describes the experimental test set-up. The second part of the paper presents the trailing-edge region velocity and vorticity fields acquired during a ramp-type deployment, including correlation with measured pressure profiles. Spectral analysis of the velocity fields captured at different AGF deployment heights reveals the AGF and trailing-edge vortex shedding frequencies, providing a useful basis for CFD validation.

1 NOMENCLATURE

α	angle of attack
c	airfoil chord
C_L	lift coefficient
δ_{AGF}	AGF deployment height
M	Mach number
S	aerodynamic time, $S = tU_\infty/c$
t	dimensional time
t_{act}	AGF actuation time
u	local streamwise velocity
U_∞	freestream velocity
ω_z	spanwise vorticity

2 INTRODUCTION

The Active Gurney Flap (AGF) concept has received significant attention from the rotorcraft research community[1-7]. The concept employs a small flap that is deployed perpendicular to the pressure side of the airfoil near the trailing-edge. The vortex structures shed from the AGF move the Kutta condition to a point aft of the trailing-edge and increase the effective camber, thereby increasing the generated lift. The lift-to-drag ratio remains favourable up to moderate Mach numbers and deployment heights of up to 2% (or in the order of the local boundary layer thickness)[8,9]. By dynamically retracting the AGF on the advancing side of the rotor disk while in forward flight, the drag penalty associated with the high local Mach numbers can be avoided. The additional lift generated by the AGF on the retreating side is used to off-load the outboard end of the rotor blade, allowing it to operate at reduced angles of attack, the intended result of which is a reduction in power consumption[3,5].

Only limited experimental results have been published on airfoils with deploying Gurney-type flaps[6,10-12]. In the work of Solivitz et al[10] Particle Image Velocimetry (PIV) measurements were

performed on a deploying flap mounted on a blunt trailing-edge. The recent experimental investigation published by Palacios et al[6] considered a novel pneumatic actuation mechanism deploying the AGF at an upstream position of 90% chord. In the current study, the AGF is positioned further downstream to increase its effectiveness and minimize potential unsteady aerodynamic effects while preserving the sharp trailing-edge geometry as much as possible. The AGF is deployed using an electromechanical actuator combined with a flexure bearing mechanism[13] designed to be suitable for sub-sequent flight testing.

The AGF concept represents one of the key technologies under development in the European Clean Sky – Green Rotorcraft program. This paper presents the first in a series of experimental activities aimed at maturing the AGF system that is planned to be flight tested at the end of the project. A full-scale 2-D rotor blade section was tested in the subsonic anechoic wind tunnel of Twente University. The modified public domain airfoil was fitted with a full-span AGF, driven by a flight representative actuator and mechanism. The objective of the test was to improve the understanding of the flow physics of a dynamically deploying upstream AGF, to provide a basis for numerical method development and to serve as an integrated functionality test of the AGF actuator and mechanism. More information on the test campaign can be found in [14].

The experimental set-up included time-resolved stereo PIV to measure the flow field in the vicinity of the AGF, as well as further downstream in the shed wake. The PIV measurements were meant to augment dynamic surface pressure measurements by providing detailed information regarding the flow field development during different deployment profiles. PIV measurements of the shed wake also provide the opportunity to estimate the drag effect of the AGF. Acoustic measurements were also performed, but have yet to be analysed.

The first part of the paper provides an overview of the experimental test set-up. The following chapter presents the results of the time-resolved PIV measurements captured during one of the ramp-type deployment test cases, focussing in particular on the flow field developments during the deployment upstroke. Next, frequency domain analysis and

Proper Orthogonal Decomposition (POD) are used to isolate the coherent flow fluctuations that dominate the flow field. Finally, PIV measurements of the airfoil shed wake were carried out to allow CFD validation of the wake development and estimation of the AGF effect on the total drag. The latter will not be discussed further in this paper since the work is still in progress.

3   EXPERIMENTAL SET-UP

The experiments were performed in the Twente University low-subsonic anechoic wind tunnel (Figure 1). The test section dimensions equal 0.9 m in width and 0.7 m in height. The maximum tunnel speed that could be achieved with the selected test section was 60 m/s. The freestream turbulence levels ranged between 0.5-0.6%.

Figure 1: Test section of the Twente University anechoic wind tunnel

The chord of the blade section equalled 0.5 m, limited by the full-scale actuator and deployment mechanism that were used for the test. The relatively large size of the test object restricted the test matrix to low incidence angles in order to avoid significant blockage and wind tunnel wall effects.

The blade section was designed and manufactured by Airborne Composites using a combination of composite and metallic parts. The boundary layer was tripped at 10% chord in order to facilitate comparisons with CFD. Furthermore, the surface was painted black with a low-reflective paint to accommodate the PIV measurements. The actuator and mechanism were developed by Microtecnica SRL, in cooperation with Bristol University[13]. The

incidence control mechanism designed by Twente University consisted of two aluminium rotating disks actuated by linear actuators on either side of the test section. The angle of incidence, fixed at each test point, was measured using calibrated inclinometers mounted on the rotating disks. The AGF control software allowed the definition of sinusoidal and ramp-type deployment schedules, including variations in the deployment speed and height. The deployment height was measured using wall-mounted Hall sensors.

The blade section was fitted with 23 dynamic pressure transducers positioned at mid-span. Kulite LQ-062 sensors were used in leading and trailing-edge regions to allow for a dense distribution. On other locations the larger Kulite LL-250 sensors were employed. In light of the limited number of sensors, the chordwise distribution (Figure 2) was optimized with respect to computed 2-D static pressure distributions in order to capture the circulatory effects as well as the pressure differential in the vicinity of the AGF.

Figure 2: Mid-span chordwise dynamic pressure transducer distribution

All sensor data was acquired by the VIPER data acquisition system at a frequency of 20.4 kHz for a duration of 30 sec per test point.

Time-resolved PIV measurements were carried out using two LaVision HighSpeedStar 5 CMOS cameras (1024px x 1024px) and a Litron LDY304 laser (30 mJ/pulse @ 1 kHz) operated at 3 kHz. The cameras were fitted with Carl Zeiss 85 mm f/1.4 objectives (f being the focal ratio), with a Kenko 2x Macro Teleplus MC7 adapter that doubles the focal distance. Recordings were performed with the aperture set to f/2.8. The laser features an integrated optical sensor, the output of which was recorded by the VIPER system to allow synchronization of the pressure measurements with the PIV frames. The flow was seeded using DEHS particle tracers (approx. 0.25 μm particle size). Image acquisition and correlation was performed using LaVision Davis 8.1 software.

Due to the fact that the PIV measurements were a late addition to the test campaign (1 month prior to testing), the test section had been designed with limited optical access. To cope with the presence of the aluminium rotating disks, the cameras were set-up in a stereo PIV configuration (Figure 3).
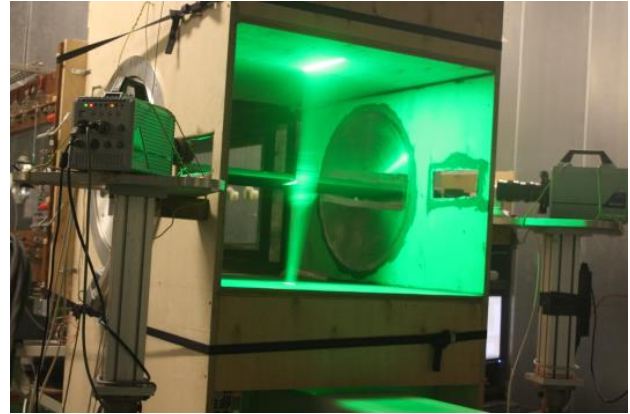

Figure 3: Photograph of the PIV set-up in stereo configuration

The laser light was introduced from below the test section. The cameras were placed on either side of the test section, at the same height as the test object, at an angle of approximately 30 degrees with the measurement plane. Scheimpflug adapters were employed to correct for the angle between object and sensor plane.

Table 1 presents a list of relevant parameters associated with the PIV set-up.

Table 1: PIV set-up parameters

Parameters	Value
Acquisition frequency	3000 Hz
Number of images	2700
Pulse separation time	6 μs
Field of view size	66 mm x 60 mm
Interrogation window size	24px x 24px
Overlap	50%
Vector resolution (dx, dy)	0.72 mm, 0.72 mm

The PIV wake measurements employed a 2-component PIV double camera setup, where the cameras were placed on one side of the tunnel. This allowed for an extended field of view of 345 mm x 200 mm centred on a position 270 mm downstream of the trailing-edge.

4 RESULTS

4.1 Time-Averaged PIV

Figure 4 presents the time-averaged flow field behind the statically retracted (top) and deployed (bottom) AGF at the maximum achievable wind tunnel speed and deployment height. The flow field is averaged over 200 frames. The shaded parts of the figure represent areas where no velocity vector data is available due to occlusion of the laser light.
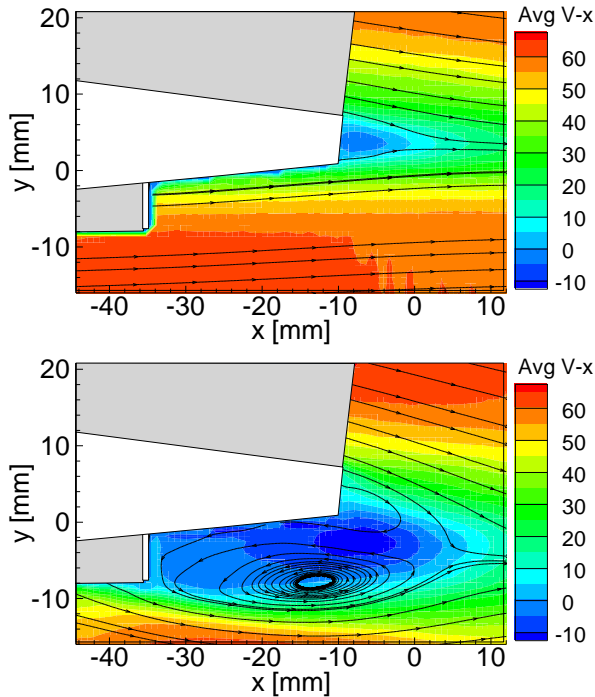

Figure 4: Streamlines and time-averaged stream-wise velocity [m/s] behind statically retracted (top) and deployed (bottom) AGF with a height of 1.3% chord

On the right hand side of the figure, the streamlines clearly illustrate the presence of a large area of average counter-clockwise vortex flow downstream of the AGF. The vortex extends from the position of the AGF until beyond the trailing-edge. At the trailing-edge there exists also a much smaller clockwise rotating vortex that entrains fluid from the suction side of the airfoil. The downstream distance at which streamlines coalesce is not greatly increased with respect to the clean (blunt trailing-edge) airfoil.

By comparing the top and bottom figures it is clear that the presence of the AGF serves to increase the streamwise velocity on the suction side of the airfoil,

while decreasing the velocity on the pressure side. The result is a net increase in circulation and therefore in lift. The effect on the circulation is also evident in the increased downward angle of the streamlines in the deployed case.

4.2 Time-Resolved PIV

Figure 5 presents the instantaneous normalized velocity (left) and vorticity (right) fields at several steps during a single ramp-type deployment at the test conditions provided in Table 2. The associated phase-averaged lift response is depicted in Figure 6. The solid dots indicate the timing of the snap shots of the velocity fields presented in Figure 5. Note that the oscillations induced by vortex shedding have been filtered out in the phase averaging process.

The corresponding pressure distributions are provided in Figure 8. The boundary layer velocity profile downstream of the AGF as captured by PIV is depicted Figure 7. The black solid lines correspond to the averaged profiles while the AGF is either retracted or deployed. Given these profiles, the boundary layer thickness of the clean airfoil (i.e. retracted AGF) equals approximately 8.6 mm in the trailing-edge region. Hence, at maximum deployment the AGF is still submerged in the boundary layer.

Table 2: Experiment test conditions

Mach [-]	α [deg]	δ_{AGF} [%]	Δt_{act} [ms]	ΔS_{act} [-]
0.18	4.0	1.4	25	2.95

The top row of Figure 2 shows the first snapshot where the initial effect of the AGF is visible in terms of a narrow region of decelerated/reverse flow near the lower side of the airfoil. Simultaneously, in the lower side of the PIV window the flow accelerates as it moves around the deploying AGF. The flow on the upper side of the airfoil has remained largely unaffected. The pressure distribution shows the localized effect of the AGF in terms of a low pressure region below the airfoil trailing-edge. The vorticity contours on the right hand side show increasing shear-induced positive vorticity aft of the deploying AGF. The circulation around the airfoil has remained largely unaffected up to this point, which is consistent with the lift coefficient and pressure distribution depicted in Figure 6 and 8, respectively.
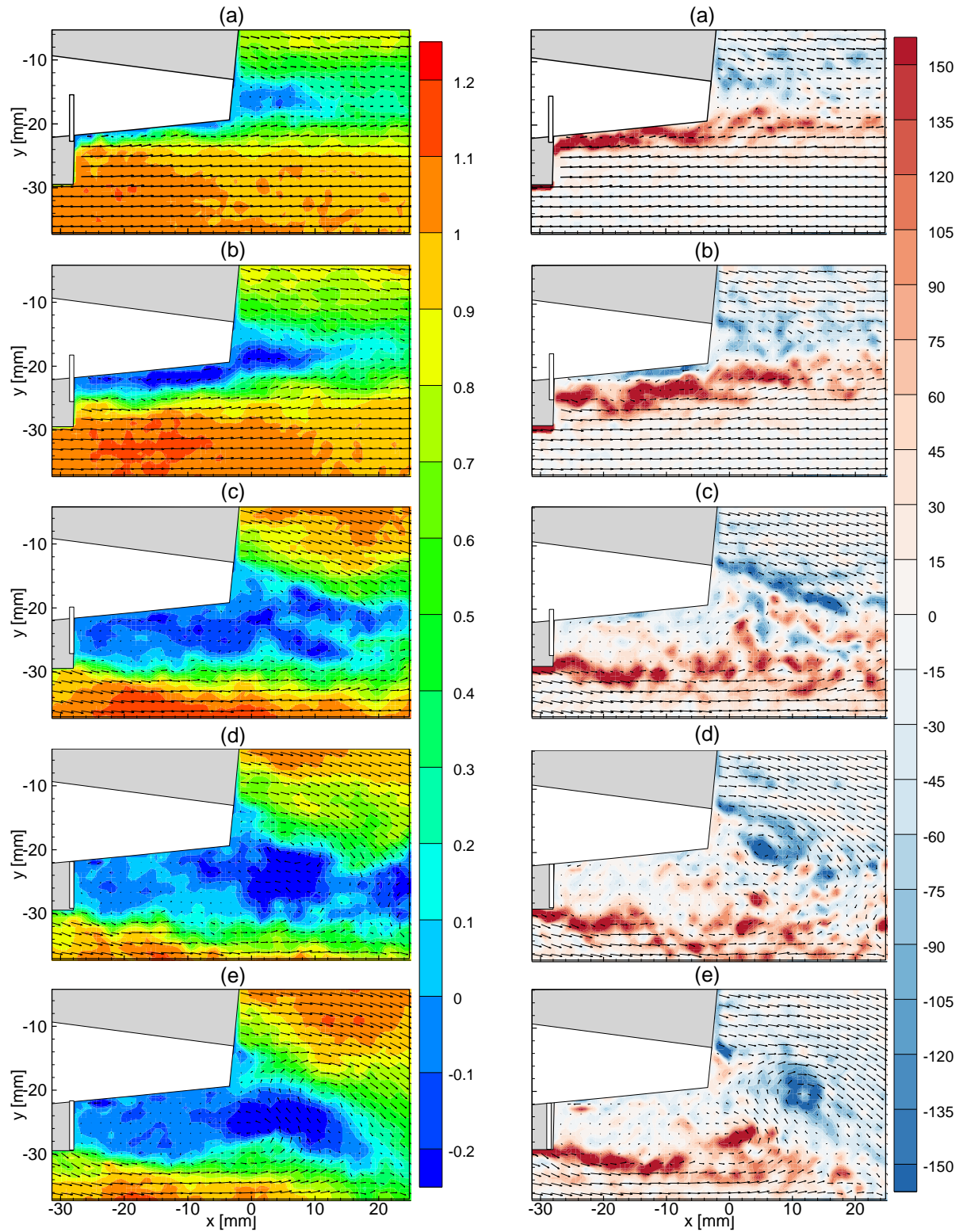
Figure 5: Instantaneous normalized streamwise velocity u/U$_\infty$ (left) and normalized spanwise vorticity $\omega_z c$/U$_\infty$ (right) during ramp-type AGF deployment.
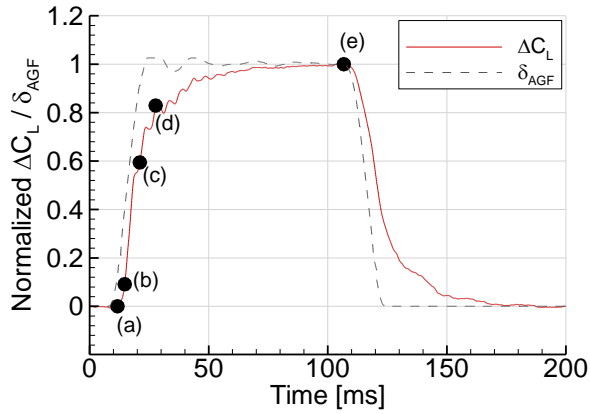
Figure 6: Measured normalized phase-averaged lift increment and deployment height during a ramp-type AGF deployment cycle.
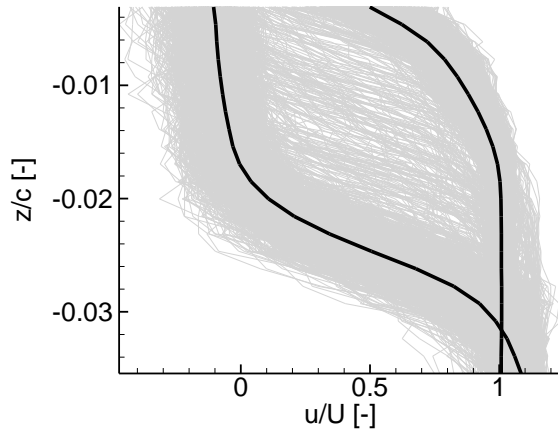

Figure 7: PIV captured boundary layer velocity profile downstream of AGF during a ramp-type AGF deployment cycle.

In the second row of the PIV frames, the region of decelerated flow has grown and now extends up to the separated flow area at the trailing-edge. The third row of figures shows the situation where the flap is more than halfway deployed. There is a significant region of reversed flow, while the velocity vectors indicate downwards flow from the suction side of the airfoil. In the fourth row, the AGF is fully deployed and the velocity field is approaching the final steady-state. Two distinct layers of vorticity are apparent, clearly indicating the separating shear layers the interaction of which is associated with the formation of the Von Karman vortex street[15]. The vorticity plot also shows the formation of a negative (clockwise) vortex through the rolling up of vorticity shed from the trailing-edge. Finally, the bottom row presents a snapshot of the steady flow at full AGF deployment. The vorticity plot shows the interaction
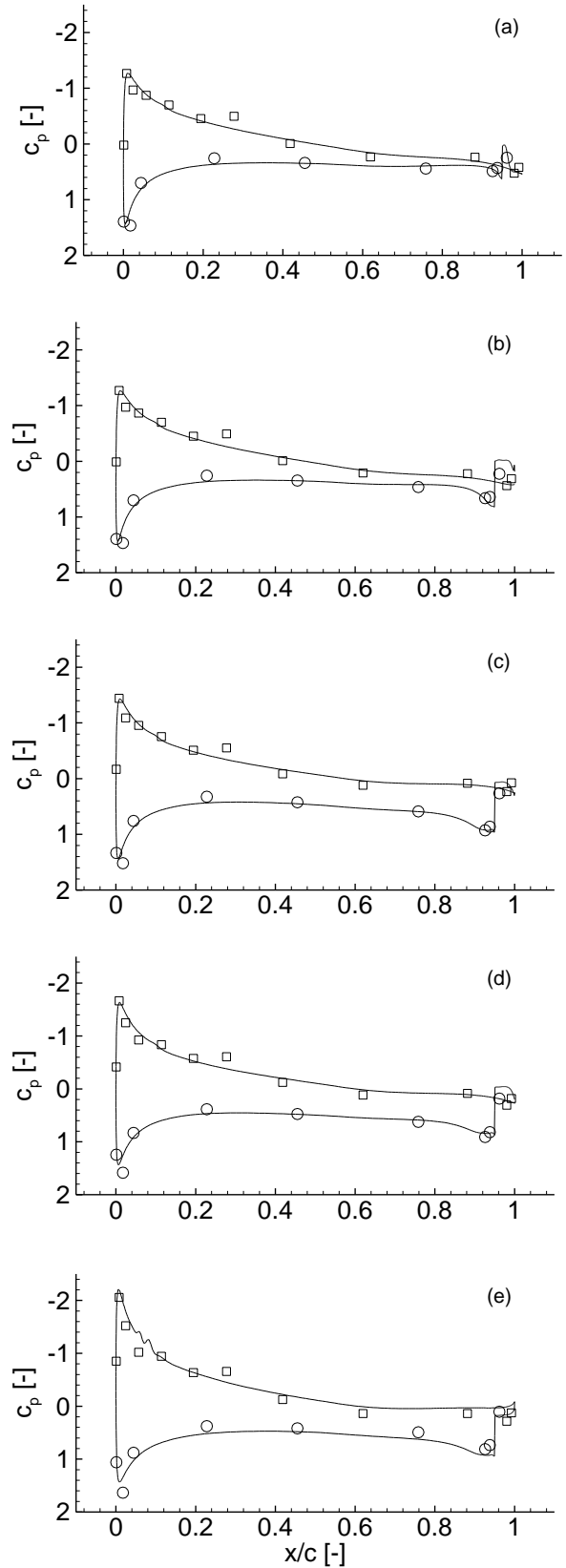

Figure 8: Phase-averaged pressure distributions during ramp-type AGF deployment (symbols: measurements, lines: CFD).

of the shear layers along with the formation and shedding of two counter-rotating vortices.

Measurements performed by Palacios[6] suggest the possibility of an initial negative lift peak developing during deployment, before the circulation around the airfoil adjusts and the AGF starts producing positive lift. The lift peak increases with deployment speed and forward placement of the AGF. In [6], the negative lift peak is associated with a vortex extending from the AGF to the trailing-edge. While the velocity fields captured by PIV do not support the presence of a vortex, the region of accelerated flow below the AGF combined with unaltered velocities at the suction side of the airfoil could translate into momentary negative lift. To test this hypothesis, the instantaneous pressure fields could be computed from the PIV data, but this is considered out of the scope for the current investigation. CFD calculations of the experiment configuration on the other hand do predict a negative lift peak, but because of the relatively large non-dimensional deployment time ($S_{act} = t_{act}U_\infty/c = 2.95$) the peak is not significant. Indeed, within the practical limits of the actuator, the initial negative lift peak is not a matter of concern from a performance perspective, especially at realistic in-flight Mach numbers.

4.3 Spectral analysis

Spectral analysis of PIV images can provide useful information concerning periodic features of a flow field. In the case of this experiment, the frequency content of the PIV data will also form the basis for a frequency domain validation of CFD computations performed by project partners[16].

The frequency spectra presented in Figure 9 reveal the vortex shedding frequency of the AGF and the blunt trailing-edge. The spectra were obtained through Fast Fourier Transformation of the streamwise velocity fluctuations for different deployment heights at $M = 0.18$ and $\alpha = 0.0$ deg. The spectrum labelled $\delta = 0.0\%$ was identified from the same PIV data as the spectrum labelled $\delta = 0.6\%$ but at a downstream vertical position close to the chordline of the airfoil in order to capture the velocity fluctuations behind the blunt trailing-edge during the retracted periods of the deployment cycle. The other spectra were identified at vertical positions corresponding to the shear layer extending from the tip of the AGF.

As the AGF deployment height is increased, so is the distance between the shear layers extending from the airfoil trailing-edge and the tip of the AGF. The period associated with the interaction between the two shear layers is increased and consequently the vortex shedding frequency is reduced. This effect is clearly seen in Figure 9 which shows response peaks at reducing frequency as the deployment height is increased. To identify the associated flow topologies, Figure 10 presents contour plots of the frequency response magnitude at 620 Hz and 1078 Hz. The former clearly corresponds to vortex shedding at the trailing-edge, while the latter is associated with vortex shedding behind the AGF. Note that similar frequency spectra have been obtained from accelerometer data acquired at various positions in the trailing-edge region.
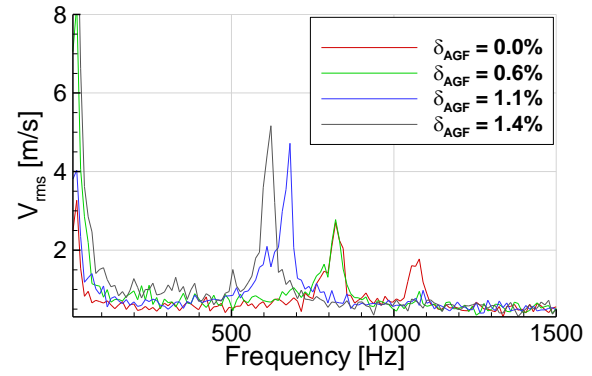

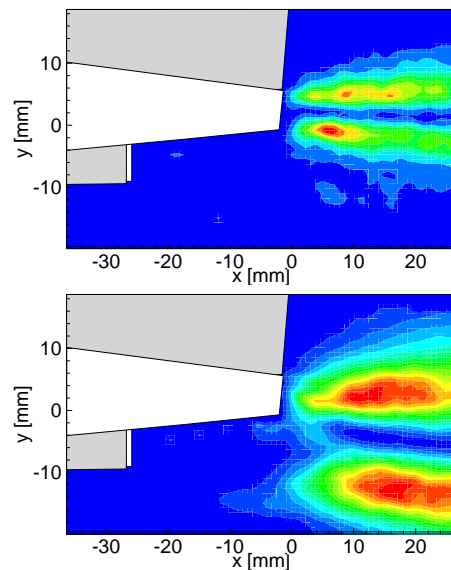**Figure 9: Frequency spectra identified from PIV images of several ramp-type AGF deployment cycles.**

Figure 10: Contour plot of frequency response magnitude at 1078 Hz (top) and 620 Hz (bottom).

4.4   Orthogonal Decomposition

Proper Orthogonal Decomposition (POD) is a statistical analysis technique that can be used for data reduction and to identify coherent fluctuations. The decomposition also filters out noise in a manner similar to phase-averaging when the measurement spans only a few cycles. POD is in essence similar to a Fourier transformation, but provides a more efficient decomposition by first identifying the natural modes of the flow. POD also facilitates the validation of CFD methods by restricting the comparison to distinct features of the flow. The POD decomposition of measurement matrix A is defined as:

$$(1) \qquad A = U\Sigma V^T$$

Matrix A contains the velocity fluctuations around the mean flow. The columns of U correspond to the eigenvectors $\underline{u}^{(i)}$ of AA^T and represent the temporal modes. The temporal modes indicate the relative contribution of each spacial mode to the instantaneous flow field at any point in time. The columns of V contain the spacial modes $\underline{v}^{(i)}$ and are computed as:

$$(2) \qquad \underline{v}^{(i)} = \frac{1}{\sqrt{\lambda_i}} A^T \underline{u}^{(i)}$$

Finally, diagonal matrix Σ contains the eigenvalues λ_i of AA^T, which indicate the amount of energy that is associated with a particular mode. In this case POD is applied to a set of five consecutive ramp-type deployment cycles. Figure 11 presents the distribution of kinetic energy amongst the first ten orthogonal modes. Clearly, the first four modes capture the most energetic part of the flow, accounting for up to 85% of the total kinetic energy.
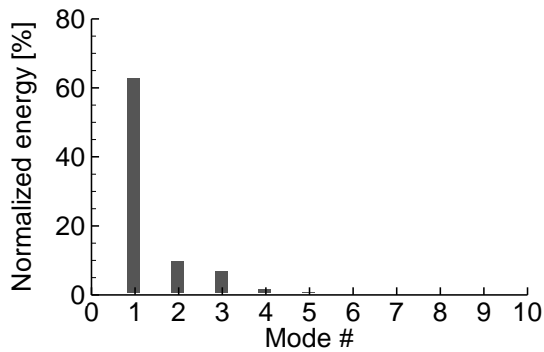

Figure 11: Normalized kinetic energy distribution in POD modes.
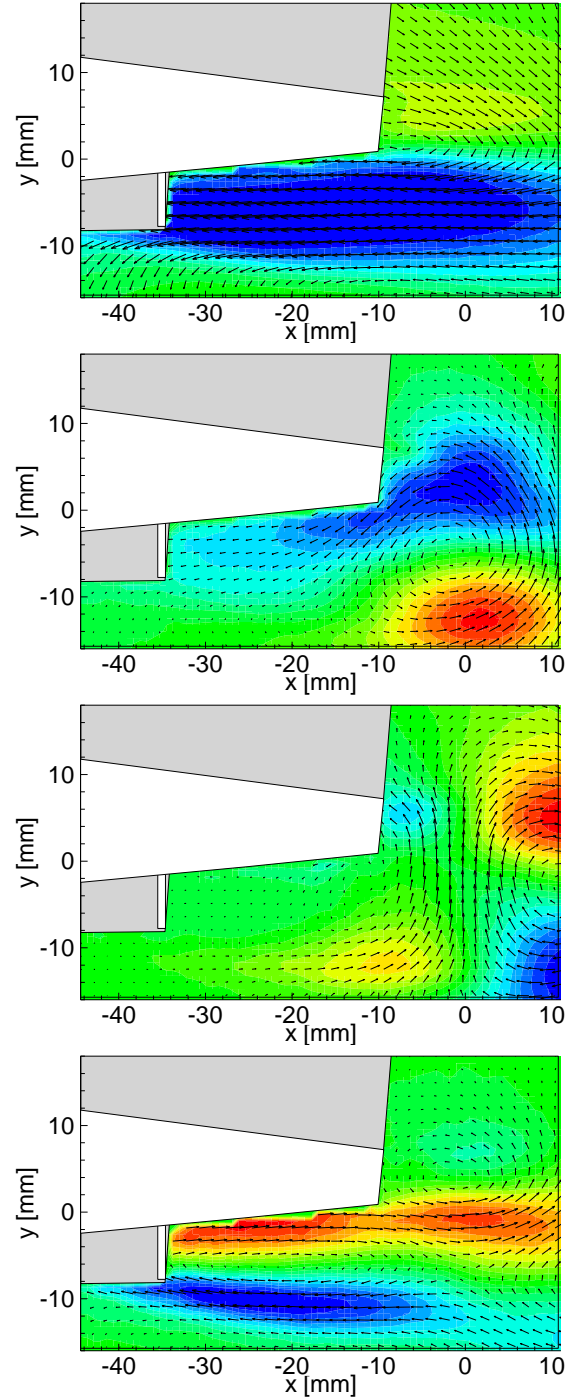

Figure 12: Dominant orthogonal modes of ramp-type AGF deployment cycle (colour contours indicate dimensionless streamwise velocity)

Figure 12 presents the velocity fields associated with the first four spacial modes, while Figure 13 plots the corresponding temporal coefficients over a single deployment cycle. The temporal coefficients clearly show that the first mode is directly related to the deployment cycle frequency.
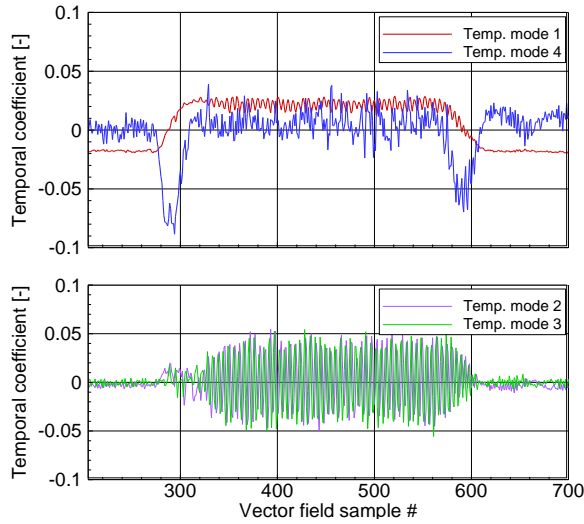
Figure 13: Temporal coefficients of dominant orthogonal modes across a single ramp-type AGF deployment cycle

The coefficient is positive while the AGF is deployed, indicating that the mode is added to the mean flow in this period, i.e. the streamwise velocity on the pressure side is decreased. The second and third modes are only active while the AGF is deployed. Considering their spacial interpretation in Figure 12, which clearly shows two vortices of opposite sign, it is evident that together these modes represent alternating vortex shedding downstream of the AGF. Finally, taking into account the negative value of the temporal coefficient, the fourth mode shows an elongated region of streamwise acceleration of the flow that is forced around the AGF and a deceleration at the root of the AGF where the flow is blocked from the freestream. The same behaviour was found in the instantaneous velocity fields captured during deployment as presented in Figure 5. The peaks in the temporal coefficients indicate that this mode is purely related to the deployment and retraction phases. The peaks coincide with the moment where the temporal coefficient of mode 1 is zero. Both peaks are of equal sign in both phases, but the retraction peak is slightly smaller and is followed by a temporary low frequency oscillation. The same pattern is found for all subsequent deployment cycles.

The relative phasing of the first three modes is depicted in Figure 14, in which the temporal coefficients of the individual modes (indicating their relative participation) are plotted against each other. The second and third modes are 90 degrees out of

phase, indicating the alternating vortex shedding that is characteristic of a Von Kármán vortex street. The phase relations with the first mode are much weaker.
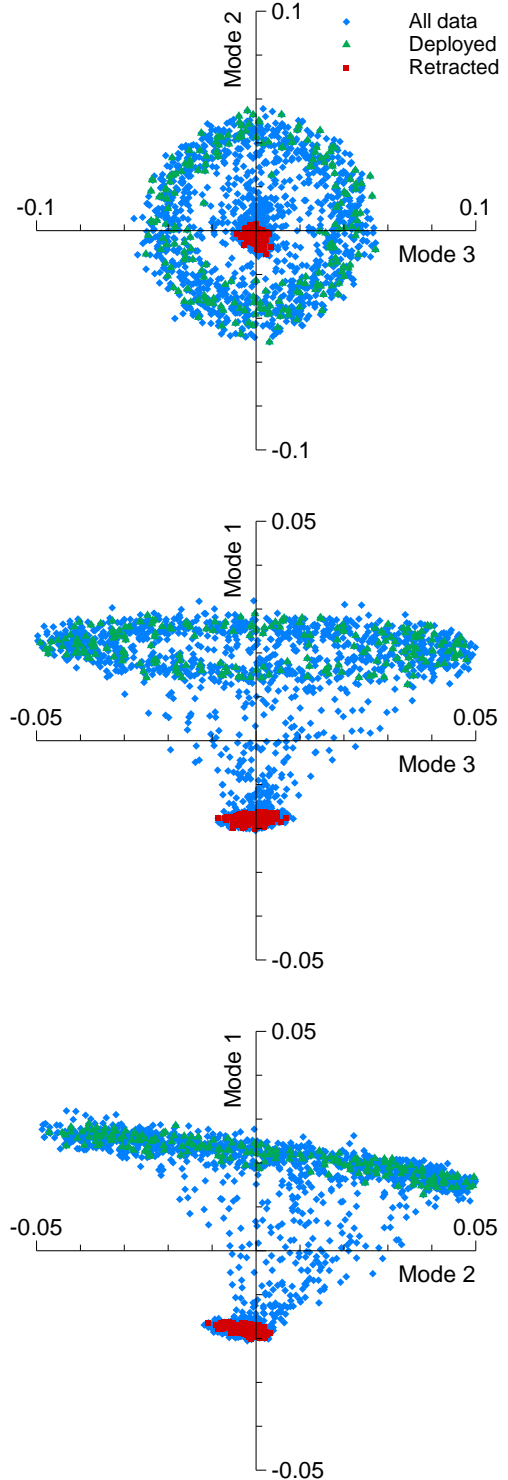

Figure 14: Phase plot of temporal coefficients of dominant orthogonal modes over multiple ramp-type AGF deployment cycles

5 CONCLUSIONS

Time-resolved PIV measurements were performed on a 2-D rotor blade section featuring a dynamically deploying AGF. Synchronization of the PIV frames with dynamic pressure measurements has provided insight into the flow mechanics behind the unsteady lift generated by a deploying upstream AGF. The initial negative lift peak measured in other experiments was not captured in the dynamic pressure measurements, but the PIV images do indicate a possible mechanism by which the lift can be temporarily reduced. However, within the practical rate limitations of the actuator, the phenomenon is not of significant consequence.

Spectral analysis of the velocity field downstream of the AGF has revealed the shedding frequencies of the blunt trailing-edge as well as the deployed AGF. The shedding frequency was found to decrease with deployment height. The frequency spectra identified for different deployment heights, rates and test conditions will form a valuable and convenient basis for the validation of CFD computations.

POD analysis was applied to identify the dominant behaviours of the flow during a ramp-type AGF deployment cycle. It was found that the flow can be accurately represented by as few as four orthogonal modes. Among these four modes are two that together capture the vortex shedding behind the AGF.

The deployment schedule is easily recognized in the evolution of the temporal coefficients associated with the first four POD modes. This allows a straight-forward qualitative identification of the AGF deployment state without requiring synchronization to other data sources.

6 FUTURE ACTIVITIES

To date, the analysis of the PIV data has considered only a small portion of the total test matrix. Future activities should therefore include a more detailed parameter investigation taking full advantage of the data available. Additionally, considering the absence of a mechanical balance or a wake survey, it will be investigated whether or not the shed wake PIV measurements can be exploited in order to estimate the effect of the AGF on the total profile drag, thereby provided additional data for CFD validation.

7 ACKNOWLEDGEMENTS

8 COPYRIGHT STATEMENT

9 REFERENCES

1. Kinzel, M.P., "Miniature Trailing-Edge Effectors for Rotorcraft Performance Enhancement", Proceedings of the American Helicopter Society 61st Annual Forum, Grapevine, Texas, May 2005, pp. 442-453.

2. Roedts, R.L and Maughmer, M.D., "Rotorcraft Performance Enhancements Due to a Lower-Surface Effector", Proceedings of the 35th European Rotorcraft Forum, Hamburg, Germany, September 2009, pp. 886-899.

3. Bae, E.S., Gandhi, F. and Maughmer, M., "Optimumly Scheduled Deployments of Miniature Trailing-Edge Effectors for Rotorcraft Power Reduction", Proceedings of the American Helicopter Society 65th Annual Forum, Grapevine, Texas, May 2009, pp. 187-211.

4. Bae, E.S. and Gandhi, F., "Upstream Active Gurney Flap for Rotorcraft Vibration Reduction", Proceedings of the American Helicopter Society 68th Annual Forum, Fort Worth, Texas, May 2012, pp. 1354-1362.

5. Van 't Hoff, S.C., Federico, L., Pavel, M.D., Visingardi A. and Van Rooij, M., "Optimization and Evaluation of an Active Gurney Flap System for Rotorcraft Performance Improvement and its Impact on Handling Qualities", presented at the 39th European Rotorcraft Forum, Moscow, Russia, September 2013.

6. Palacios, J., Kinzel, M. and Overmeyer, A., "Active Gurney Flaps: Their Application in a Rotor Blade Centrifugal Field", Journal of Aircraft, Vol. 51(2), 2014, pp. 473-489.

7. Spurway, S., "Clean Sky Programme: an Overview of the Active Gurney Flap Programme", presented at the AAAF/CEAS Greener Aviation Conference, Brussels, Belgium, March 2014.

8. Liebeck, R.H., "Design of Subsonic Airfoils for High Lift", Journal of Aircraft, Vol. 15(9), pp. 547-561, 1978.

9. Giguère, P, Dumas, G. and Lemay, J., "Gurney Flap Scaling for Optimum Lift-to-Drag Ratio", AIAA Journal, Vol. 35(12), pp.1888-1890, 1997.

10. Solovitz, S.A. and Eaton, J.K., "Dynamic Flow Response Due to Motion of Partial-Span Gurney-Type Flaps", AIAA Journal, Vol. 42(9), September 2004.

11. Tang, D. and Dowell, E.H., "Aerodynamic Loading for an Airfoil with an Oscillating Gurney Flap", Journal of Aircraft, Vol. 44(4), 2007.

12. Matalanis, C.G., Wake, B.E. Opoku, D., Min, B.Y., Yeshala, N. and Sankar, L., "Aerodynamic Evaluation of Miniature Trailing-Edge Effectors for Active Rotor Control", Journal of Aircraft, Vol. 48(3), 2011.

13. Freire Gómez, J., Booker, J.D., Mellor, P., "Design and Development of an Active Gurney Flap for Rotorcraft", proceedings of SPIE Smart Structures/NDE Conference, San Diego, USA, March 2013.

14. Loendersloot, R., Freire Gómez, J. and Booker, J.D., "Wind Tunnel Testing of a Full-Scale Helicoper Blade Section with an Upstream Active Gurney Flap", presented at the presented at the 40th European Rotorcraft Forum, Southampton, Britain, September 2014.

15. Gerrard, J. H., "The Mechanics of the Formation Region of Vortices Behind Bluff Bodies," Journal of Fluid Mechanics, Vol. 25(2), June 1966.

16. Baverstock, K., "AgustaWestland's Application of HMB to Simulate the Active Gurney Flap", presented at the presented at the 40th European Rotorcraft Forum, Southampton, Britain, September 2014.